npj | computational materials

Article

Published in partnership with the Shanghai Institute of Ceramics of the Chinese Academy of Sciences

https://doi.org/10.1038/s41524-025-01619-0

Multidimensional coherent spectroscopy of correlated lattice systems

Jiyu Chen & Philipp Werner ✉

Multidimensional coherent spectroscopy (MDCS) has been established in quantum chemistry as a powerful tool for studying the nonlinear response and nonequilibrium dynamics of molecular systems. More recently, the technique has also been applied to correlated electron materials, where the interplay of localized and itinerant states makes the interpretation of the spectra more challenging. Here we use the Keldysh contour representation of effective models and nonequilibrium dynamical mean field theory to systematically study the MDCS signals of prototypical correlated lattice systems. By analyzing the current induced by sequences of ultrashort laser pulses we demonstrate the usefulness of MDCS as a diagnostic tool for excitation pathways and coherent processes in correlated solids. We also show that this technique allows to extract detailed information on the nature and evolution of photo-excited nonequilibrium states.

The development of ultrashort laser pulses enabled experimental studies of the nonequilibrium properties of many-body quantum systems on their intrinsic timescales[1–3]. Time-resolved pump-probe spectroscopy has become a standard tool for exploring the response of correlated electron materials to interband charge excitations, the transient Floquet states realized under periodic driving, as well as the relaxation and thermalization processes[4,5]. However, heating effects can obscure interesting phenomena, while nonequilibrium processes with multiple pathways can be difficult to disentangle using traditional approaches. To gain deeper insights into the dynamics of many-body systems, it is thus important to develop techniques which employ weak pulses, and which can distinguish between different excitation and relaxation pathways.

Multidimensional coherent spectroscopy (MDCS) is capable of revealing nonlinear responses of atomic or molecular systems, as well as the out-of-nonequilibrium dynamics in chemical reactions and protein folding[6–8]. A more recent trend is the extension of this technique to lattice systems. A broad range of materials has been explored with pulses from the Terahertz[9–15] to the optical range[16–18], while theoretical studies of MDCS have so far mainly focused on spin systems, few-site clusters or one-dimensional models[19–29]. In this article, we show how MDCS can be used to study the equilibrium and nonequilibrium properties of high dimensional strongly correlated electron systems. By simulating multi-pulse MDCS measurements for prototypical lattice models using nonequilibrium dynamical mean-field theory (NEQ-DMFT)[30], we demonstrate that weak optical excitations can reveal the nature of correlated states, the interaction strengths, the relaxation of excited states, as well as coherent quantum phenomena in strongly correlated materials.

Results

Multi-pulse setup

Conventional transient absorption experiments involve two pulses – a pump pulse drives the system into an excited state, while the following probe pulse is used to detect the pump-induced modifications in the sample. The tunable time delay between the pump and the probe pulse allows to track the dynamics of these changes (Fig. 1a). While these and other pump-probe experiments provide important insights into the nonequilibrium dynamics[5], conventional pump-probe experiments have some limitations when it comes to detecting fine and transient structures during the ultrafast evolution of the system. The typically strong pump pulse required to generate a detectable difference in the probed signal will heat the system, or even degrade the lattice structure[31]. Also, strong interband charge transfers and incoherent backgrounds can hide short-lived transient high energy states or coherent dynamics in strongly correlated materials[32,33].

In the common four-wave-mixing MDCS setup, three phase matched non-collinear pumps are applied to excite the sample in a "box" geometry (Fig. 1b). By alternating the order of the pump sequences, different excitation pathways can be studied[34]. In photo-current spectroscopy (Fig. 1c), the optical pumps are combined with electric current detection. This approach can effectively explore the low-fluence regime, suppress background signals and improve the spatial resolution[35]. In this work, we consider a similar protocol to simulate and analyze the two-dimensional coherent spectra (2DCS) of prototypical correlated lattice models. We use a fully collinear setup combining three phase-stable broadband (monocycle femtosecond) laser pulses with a direct detection of the induced current signal. The relative time delays τ, T and t between the pulses can be precisely controlled (Fig. 1c). To study the transient 2DCS signal of a photo-doped nonequilibrium system, we excite the system with an additional strong pulse which acts before or during the sequence of weak monocycle pulses (time delay t_{ph}). The third order response is obtained by subtracting the single-pulse and two-pulse contributions to the measured signal. A two-dimensional Fourier transformation within the multi-dimensional time delay space (t_{ph},τ,T,t) transforms (τ,t) into (ω_τ, ω_t). The dependence of the 2DCS signal on t_{ph} and T

Department of Physics, University of Fribourg, 1700 Fribourg, Switzerland. ✉e-mail: philipp.werner@unifr.ch

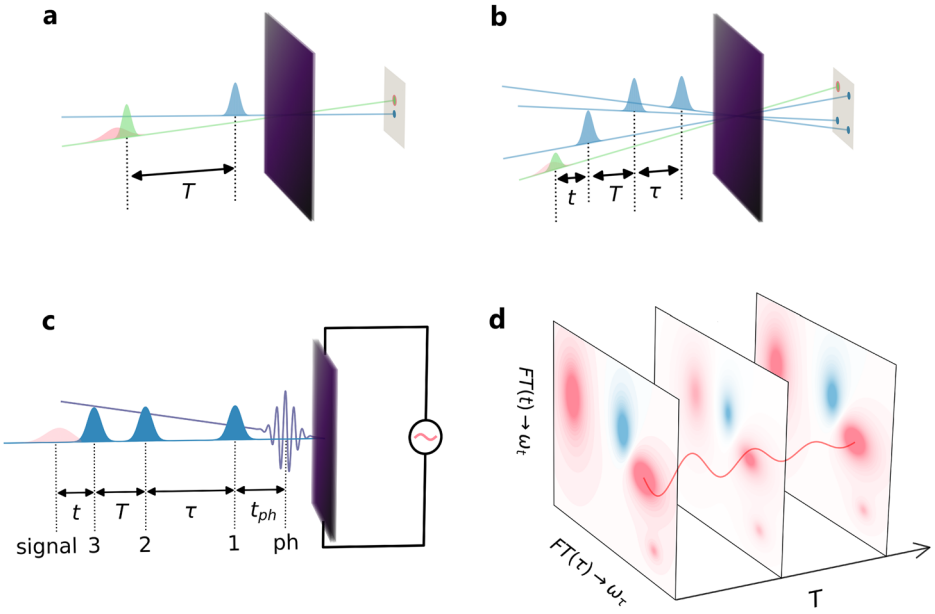

Fig. 1 | Multi-pulse setups for pump-probe spectroscopy and MDCS. a Two-pulse setup in a pump-probe experiment. The pump (blue) and probe (green) pulses are separated by a delay time T. **b** Four wave mixing realization of MDCS. Four non-collinear pulses with relative time delays τ, T and t form a box-geometry. In an optical measurement, the signal (red) is heterodyned with the last pulse (green). **c** MDCS setup with three collinear pulses (blue) and optical current measurement. An additional pump excitation (purple) at time t_{ph} before the three blue-shaded pulses can be added to photodope or drive the system into a nonequilibrium state. The signal (red) is collected by an electric measurement. **d** A twodimensional Fourier transformation converts the time delay (τ, t) into (ω_τ, ω_t). The signal intensities change as a function of the time delay T.

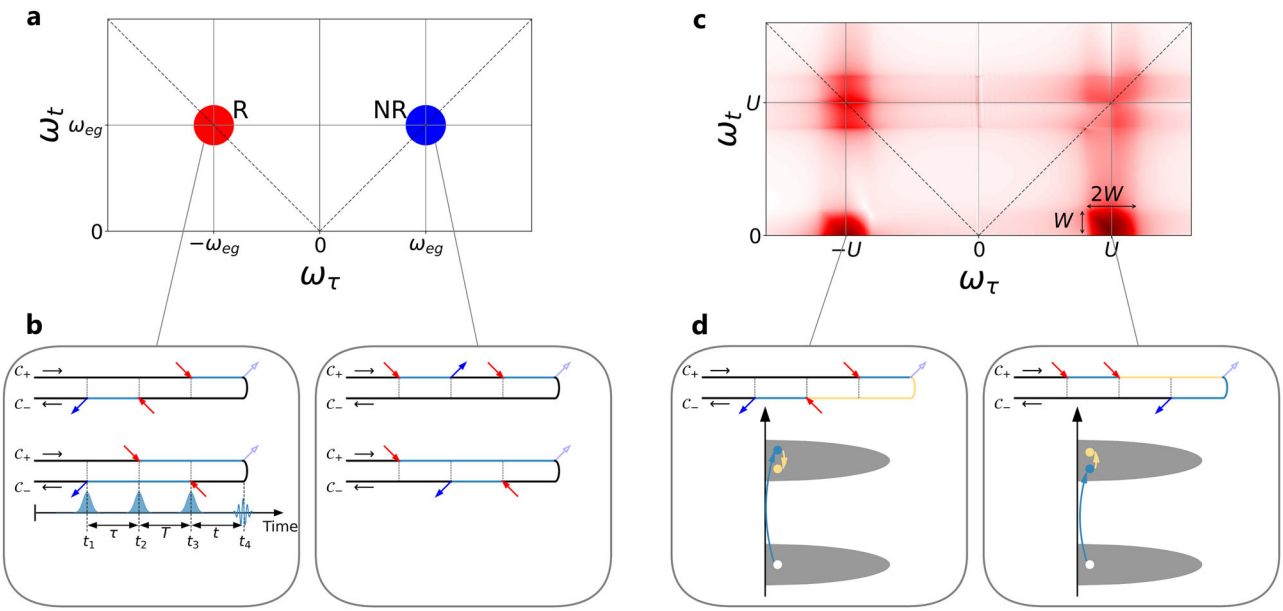

Fig. 2 | 2DCS of a two-level system and a single-orbital Mott insulator. a R (red) and NR (blue) signals of a two level system with energy splitting ω_{eg}, showing up in the (− , +) and (+ , +) quadrant of the (ω_τ,ω_t) domain. **b** Keldysh diagrams illustrating the excitation and deexcitation pathways associated with the three laser pulses (blue and red arrows). The colors of the contour segments indicate the state of the system (black: ground state, cyan: excited state). The real time intervals τ, T and t between the three pulses and the measured signal (dashed arrow) are indicated in the bottom left subpanel. **c** Hubbard model results for local interaction U, with on-diagonal R and NR signals due to inter-Hubbard-band excitations and additional 2Q signals associated with intra-Hubbard band excitations. **d** Keldysh diagrams and sketches of the 2Q process. Only the diagrams with the intra-Hubbard band excitation on the upper branch are shown.

allows to track the evolution and decoherence of nonequilibrium states (Fig. 1d).

Keldysh contour analysis

We simulate MDCS measurements of high-dimensional correlated lattice systems with NEQ-DMFT, which is based on the nonequilibrium Green's function formalism[30]. Figure 2b depicts the coherent evolution of the density matrix of a simple two-level system on the two-branch Keldysh contour $\mathcal{C} = \mathcal{C}_+ \cup \mathcal{C}_-$. This contour representation is related to the double-sided Feynman diagrams in Liouville space[6,36], but more familiar to researchers with a condensed matter background. The arrows along the Keldysh contour mark the excitations and deexcitations of the system, while the colors of the contour segments represent the evolution of the many-body state. The three pumps induce a third-order response proportional to $S^{(3)}(\tau,T,t) \propto \langle[[[\hat{\boldsymbol{j}}(0),\hat{\boldsymbol{j}}(\tau)],\hat{\boldsymbol{j}}(\tau+T)],\hat{\boldsymbol{j}}(\tau+T+t)]\rangle$ (or $S^{(3)}(t_1,t_2,t_3,t_4) \propto \langle[[[\hat{\boldsymbol{j}}(t_1),\hat{\boldsymbol{j}}(t_2)],\hat{\boldsymbol{j}}(t_3)],\hat{\boldsymbol{j}}(t_4)]\rangle]$), where $\hat{\boldsymbol{j}}$ denotes the current operator. The three nested commutators generate eight interaction pathways, forming three groups of signals which we denote as rephasing (R, or echo), non-rephasing (NR) and two-quantum (2Q) signals, following the convention in ref. 8. For a detailed derivation of the nonlinear current resulting from the light-matter interaction, see Supplementary Note 4.

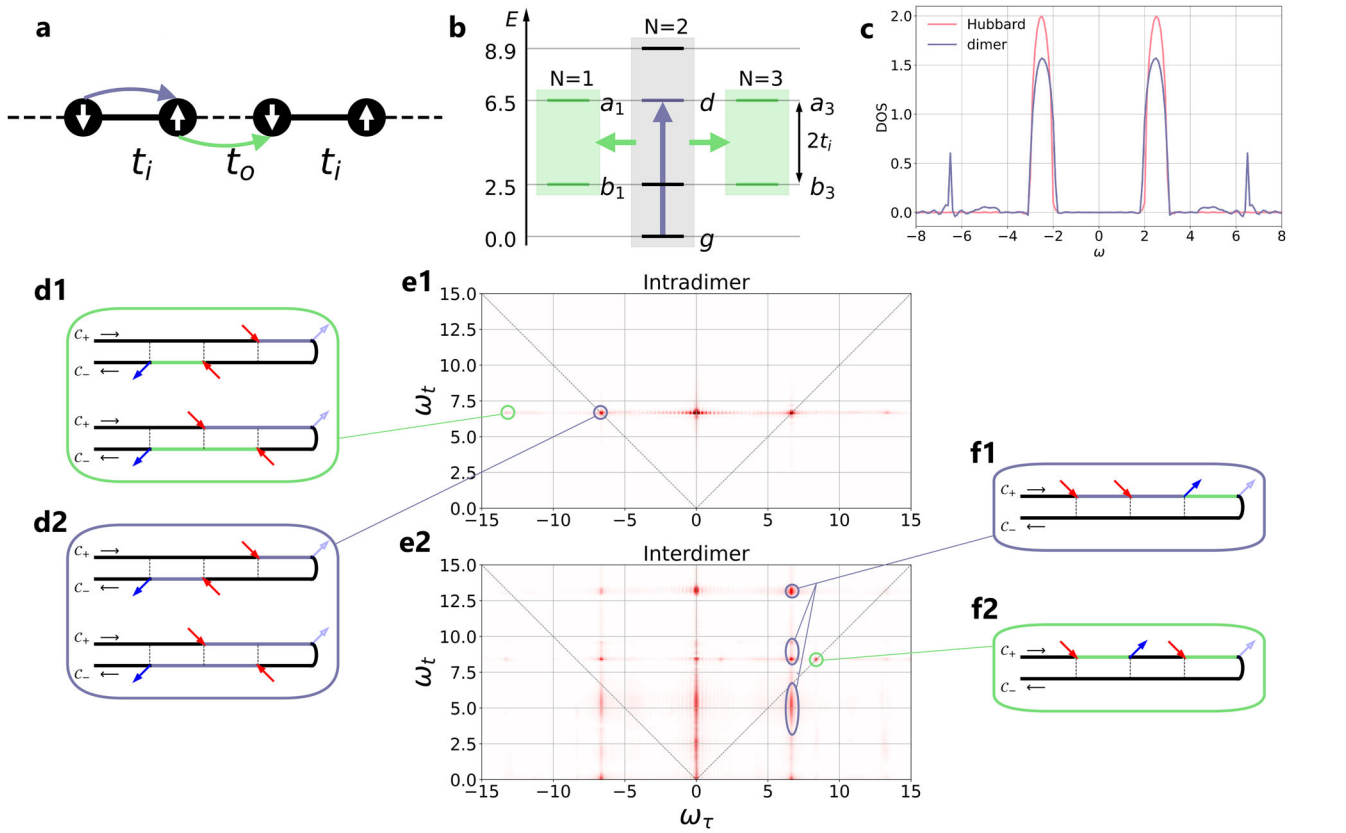

Fig. 3 | 2DCS of a correlated band insulator. a Sketch of the correlated dimer model. The solid bonds with hopping t_i form dimers, while the dashed bonds with hopping t_o connect adjacent dimers. Excitations within the dimer (purple arrow) create a doublon/holon state on the dimer. **b** Charge excitations between dimers (green arrow) create triply occupied and singly occupied dimers, with additional electrons or holons in the antibonding or bonding states. **c** Interacting density of states of the Mott insulating single band Hubbard model (red) and the dimerized correlated band insulator (blue). **e** 2DCS signal from the intradimer (**e1**) and interdimer (**e2**) current for the correlated dimer model. We use different color ranges since the intensity of the intradimer signal is larger than that of the interdimer signal. **d**, **f** Keldysh diagrams for the indicated features in the interdimer 2DCS signal.the charge gap is a correlated hybridization.

In our two-level system with ground state $|g\rangle$ and excited state $|e\rangle$ (energy difference ω_{eg}), the three pumps (solid arrows) excite $|g\rangle \rightarrow |e\rangle$ (red) or deexcite $|e\rangle \rightarrow |g\rangle$ (blue) along the Keldysh contour $\mathcal{C}$. By convention, we fix the signal emission (de-excitation $|e\rangle \rightarrow |g\rangle$, light blue arrow) at the end of $\mathcal{C}_+$. In the upper left diagram of Fig. 2b, the pump at time t_3 on the $\mathcal{C}_+$ branch excites the system from $|g\rangle$ to $|e\rangle$, while the signal emission at t_4 deexites it back to $|g\rangle$, so that the system accumulates a phase $\exp(-i\int_{t_3}^{t_4}\omega_{eg}ds) = \exp(-i\omega_{eg}t)$. On the $\mathcal{C}_-$ branch, the excitation at time t_2 is followed by the de-excitation back to $|g\rangle$ at t_1, which yields an additional phase $\exp(-i\int_{t_2}^{t_1}\omega_{eg}ds) = \exp(i\omega_{eg}\tau)$. The Fourier transformation of the total accumulated phase $\exp[-i\omega_{eg}(t-\tau)]$ produces a signal at $(-\omega_{eg}, \omega_{eg})$ on the anti-diagonal in the (ω_τ, ω_t) domain. A similar analysis can be performed for the remaining three diagrams in Fig. 2b, and the contributions can be grouped into rephasing (R) and nonrephasing (NR) signals appearing in the $(-,+)$ and $(+,+)$ quadrant, respectively (Fig. 2a). In the presence of band broadening, the NR signals are weakened compared to the R signals (Supplementary Note 5).

The qualitative features of this simple two-level system are also found in the 2DCS signal of a Mott insulating single-band Hubbard model with local interaction U larger than the bandwidth W. As shown in Fig. 2c, the spectrum for the Hubbard model features (broadened) R and NR peaks at $\omega_\tau \approx \pm U$ and $\omega_t \approx U$. In addition, this measurement produces 2Q signals at $\omega_\tau \approx \pm U$ and $\omega_t \lesssim W$, representing the excitation and deexcitation processes within the Hubbard bands. 2Q signals correspond to diagrams where the first two pumps along the real time axis interact with the system on the same branch (Fig. 2d). A weaker (stronger) first excitation ω_τ populating states at the lower (upper) edge of the upper Hubbard band, allows for larger in-band excitations (deexcitations). Consistent with this, a close inspection of the intensities of the 2Q signals in Fig. 2c shows that the largest signal appears along a line with negative slope in the (ω_τ, ω_t) plane. This effect is even more pronounced in a system with a larger bandwidth W, as shown in Supplementary Fig. 1.

In lattice systems with multiple orbitals per site or unit cell, the more complex electronic structure results in numerous excitation and relaxation pathways, coherences, and intermediate states with different characteristic lifetimes, as we will demonstrate with the following examples.

Revealing the nature of a correlated insulator

Scanning tunneling microscopy, optical conductivity and photoemission spectroscopy measurements can reveal the density of states (DOS), gap sizes and band structures of strongly correlated materials. However, in some systems, like the layered polaronic insulator 1T-TaS_2 or the Peierls distorted system VO_2, dimerizations of atoms or modulations in the stacking arrangement lead to a nontrivial interplay of band-insulating and Mott insulating characteristics[33,37–40]. Determining the nature of an insulator from the density of states alone is usually not possible. Here we demonstrate that 2DCS measurements yield clearly distinct signals for a Mott insulator and a correlated band insulator.

The 2DCS signal of a pure Mott insulator (single-band Hubbard model with interaction $U = 5$ and bandwidth $W = 4v$, $v = 0.25$) has been shown in Fig. 2c, and the corresponding single-particle spectral function is plotted by the red line in Fig. 3c. The spectral function features a gap of size $U - W = 4$. A very similar spectral function can be obtained in a correlated dimer setup inspired by the bilayer stacking arrangement in 1T-TaS_2[41], see blue line in Fig. 3c (the realistic material corresponds to a unit of energy of approximately 0.1 eV). In this system, the charge gap is a correlated hybridization

gap[39,40], controlled by excitations between bonding/antibonding states. We use a cluster DMFT setup with intradimer (interdimer) hoppings $t_i = 2$ ($t_o = 0.45$) and onsite interaction $U = 4$. The resulting DOS has two main peaks separated by $\sqrt{U^2 + 16t_i^2} - U = 4.9$ and a similar bandwidth as in the single band Hubbard model.

The 2DCS signal for the correlated band insulator, shown in Fig. 3e, differs significantly from that of the Mott insulator. We show two spectra corresponding to the intra-dimer (Fig. 3e1) and inter-dimer (Fig. 3e2) currents. The intra-dimer signal has dominant R and NR peaks at $(\omega_\tau, \omega_t) = (\pm 6.7, 6.7)$. The energy $\Delta E = (\sqrt{U^2 + 16t_i^2} + U)/2 = 6.5$ corresponds to the creation of a doublon/holon pair within a dimer (purple arrows in Figs. 3a, b), and the increase to 6.7 is the effect of the small inter-dimer hopping t_o. The Keldysh diagrams for the R peak are shown in Fig. 3d2. In addition, there are satellites at $(\omega_\tau, \omega_t) = (\pm 13.2, 6.7)$ which involve inter-dimer charge excitations from/to the ground state (see green arrows in Fig. 3a, b and the Keldysh diagrams in Fig. 3d1).

The inter-dimer 2DCS signal has a rich structure which reveals additional excitation and deexcitation processes. Let us focus on the column of peaks at $\omega_\tau = 6.7$ in the NR quadrant. This excitation energy indicates a coupling of the inter-dimer current to the intra-dimer doublon/holon processes. While the state after the first two pulses is still dominated by $N = 2$ dimers, inter-dimer hopping then produces charge excitations ($N = 2, N = 2$) $\rightarrow$ ($N = 1$, $N = 3$) to bonding/antibonding states with energy splittings of roughly $\Delta E = 5, 9, 13$ relative to the ground state (Fig. 3b, f1). The three peaks marked by the purple ovals in Fig. 3e2 represent inter-dimer singlon-triplon annihilation processes which bring the system back to the ground state. Here, the middle peak is split into two subpeaks at $\omega_t = 8.4$ and 9.6 by the effect of the inter-dimer hopping t_o. The signal at $\omega_t < 0.5$ reflects intra-band excitation/deexcitation processes.

There are additional peaks in this quadrant which have a simple interpretation. For example the peak at $(\omega_\tau, \omega_t) = (8.4, 8.4)$ corresponds to the sequence of inter-dimer charge excitation processes sketched in Fig. 3f2, which involves direct charge excitations to/from the intermediate energy manifold of the singlon-triplon pairs ($N = 1$, $N = 3$). Similarly, the signal at $(\omega_\tau, \omega_t) = (13, 13)$ involves the high-energy manifold. The signals with $\omega_\tau \approx 0$ in Fig. 3e2 (Fig. 3e1) must correspond to intra-dimer (inter-dimer) excitation processes which do not directly couple to the inter-dimer (intra-dimer) current.

Coherence in multi-orbital systems

Most strongly correlated materials host multiple active orbitals. The nontrivial interplay of bandwidths, crystal field splittings, Hubbard and Hund interactions complicates the interpretation of experimental results and the choice of appropriate parameters for numerical calculations. Here, we show that 2DCS signals of multi-orbital lattice systems allow to extract the interaction parameters and the decoherence times of excited states.

We study a two-orbital Hubbard model with Coulomb interaction U, Hund coupling J, crystal field splitting Δ and orbital-diagonal hopping v,

$$\begin{aligned}\hat{H} = &-\sum_{\langle ij\rangle,a,\sigma} v\hat{c}^\dagger_{ia\sigma}\hat{c}_{ja\sigma} + \sum_{i,a} U\hat{n}_{ia\uparrow}\hat{n}_{ia\downarrow} \\ &+ \sum_{i,a>b}(U-2J)\hat{n}_{ia}\hat{n}_{ib} - \sum_{i,a>b,\sigma} J\hat{n}_{ia\sigma}\hat{n}_{ib\sigma} \\ &+ \sum_{i,a>b}\Delta(\hat{n}_{ia} - \hat{n}_{ib}) - \mu N.\end{aligned} \quad (1)$$

Here, $n_{ia\sigma}$ denotes the occupation of orbital a at site i with electrons of spin σ, $n_{ia} = n_{ia\uparrow} + n_{ia\downarrow}$, and the sum in the first term is over nearest-neighbor sites. We solve the lattice model on an infinite-dimensional Bethe lattice, with a rescaled hopping parameter $v = 0.1$ corresponding to a bandwidth $W = 4v = 0.4$ (same for both orbitals). The interactions are chosen as $U = 4$ and $J = 0.7$. The procedure described in ref. 42 is used for the simulation of electric field pulses. We place ourselves close to the spin-state transition between the low-spin (LS) and high-spin (HS) insulating phases[43] in a system with $\Delta = 2.35$ and choose the chemical potential μ corresponding to half filling.

For the analysis of the data, it is useful to consider a simple few-level scheme which captures the relevant quasi-local processes. In Fig. 4a, we sketch the ground state manifold (g), which contains all the nearly degenerate high-spin and low-spin doublon states, excited states (e_1, e_2) with excitation energies $\omega_{e_1} = U - 2J$ and $\omega_{e_2} = U + J$, second-order excitations (d_1, d_2) with an additional cost of J and $3J$, and a high energy state h. The two possible direct excitations to e_1 and e_2 yield the diagonal peaks at $(\omega_\tau, \omega_t) = (\pm 4.7, 4.7)$ and $(\pm 2.6, 2.6)$ for the R/NR pathways (Fig. 4b). The cross peaks at $(\pm 4.7, 2.6)$ and $(\pm 2.6, 4.7)$ demonstrate the coupling of e_1 and e_2 through the ground states g or the high energy state h.

In Fig. 4c–g, we show R, NR and 2Q signal intensities as a function of T, together with the corresponding Keldysh contour diagrams. The R signals have clean features. The off-diagonal cross peaks (Fig. 4e) oscillate at the frequency of $\omega_{e1e2} = 2.1$, since two of the diagrams are in a superposition state during T. The diagonal signals (Fig. 4f) show a nonoscillating decay, since the system is in a population state $|e\rangle\langle e|$ or $|g\rangle\langle g|$ during the interval T. In contrast, the NR signals oscillate with multiple frequency components (Fig. 4c, d), due to their nonrephasing nature.

The feature located at (2.6, 0.7) (Fig. 4g) is a 2Q signal. As revealed by the Keldysh contour analysis, the first excited state e_1 undergoes an additional Hund excitation involving the formation of an interorbital LS state (d_1) with $\omega_{e_1 d_1} = J = 0.7$ (yellow arrow on the left side of Fig. 4a). During the T interval, the local state is a superposition state $|d_1\rangle\langle g|$, whose intensity oscillates at the frequency $E_{d_1} - E_g = 3.3$ (Fig. 4g). The signals with energies below $\omega_t < 0.4$ represent excitation/deexcitation processes within the band. By combining such analyses of the dominant signals in the 2DCS spectrum, the interaction parameters U and J of the simulated model can be determined.

In the strongly correlated regime $U/W \gg 1$, the life-time T_p of photo-excited charge carriers, which scales $\propto \exp[U/W]$[44], is much longer than the time range of our simulations. While this life-time has been studied both experimentally and theoretically[45,46], the decoherence time T_d of the charge carriers has not been accessible before. The decay of the intensities of the 2DCS signals during the waiting time T allow us to extract T_d. In Supplementary Tabel 1, we list the coherence times obtained from fits to the NEQ-DMFT data. These times are comparable to the inverse hopping time $\hbar/v \equiv v^{-1} = 10$. Note that the signals decay to a nonzero constant, representing the populated state with a much longer lifetime T_p.

Transient 2DCS of a photo-doped insulator

2DCS can also be used to study out-of-equilibrium systems, for example, molecular systems after a strong (actinic) laser excitation[47]. Here, we demonstrate the power of the method by considering a photo-doped Mott insulator. The additional photo-doping pulse is applied to the system a time $t_{\rm ph}$ before the three phase stable pumps of the 2DCS measurement (Fig. 1c).

We consider the half-filled two-orbital Hubbard model (Eq. (1)) without crystal field splitting ($\Delta = 0$). The other parameters ($U = 4$, $J = 0.7$, $v = 0.1$) are the same as in the previous example. The ground state g corresponds to the HS insulator (Fig. 5d). Focusing on nearest-neighbor hopping processes, the photo-doping pulse can only generate a single type of excitation, from high-spin doublons to a singlon-triplon pair (excited state e), at an energy cost of $U + J$. The 2DCS pulse sequence is applied before, during and after the photo-doping pulse to trace the excitation process and the relaxation of the system into a transient nonequilibrium state. As a reference, Fig. 5a shows the equilibrium 2DCS signal. In addition to the diagonal peaks at $(\omega_\tau, \omega_t) = (\pm 4.7, 4.7)$, there exist cross peaks located at $\omega_t = 2.1, 0.7$, representing excited state transitions to doubly excited states d_1 or d_2 (Fig. 5d) at the cost of J or $3J$. The feature at $(\omega_\tau, \omega_t) = (\pm 4.7, 6.6)$ results from an excited state with energy $2U - 2J$ relative to e. Such a state can be reached for example by a hop of the middle spin down in configuration e to the right. In addition, there is a signal close to $\omega_t = 0$, representing intra-band excitation and deexcitation processes.

In Fig. 5g, we plot difference-2DCS spectra (with the equilibrium signal subtracted) for the indicated delay times $t_{\rm ph}$ between the photo-

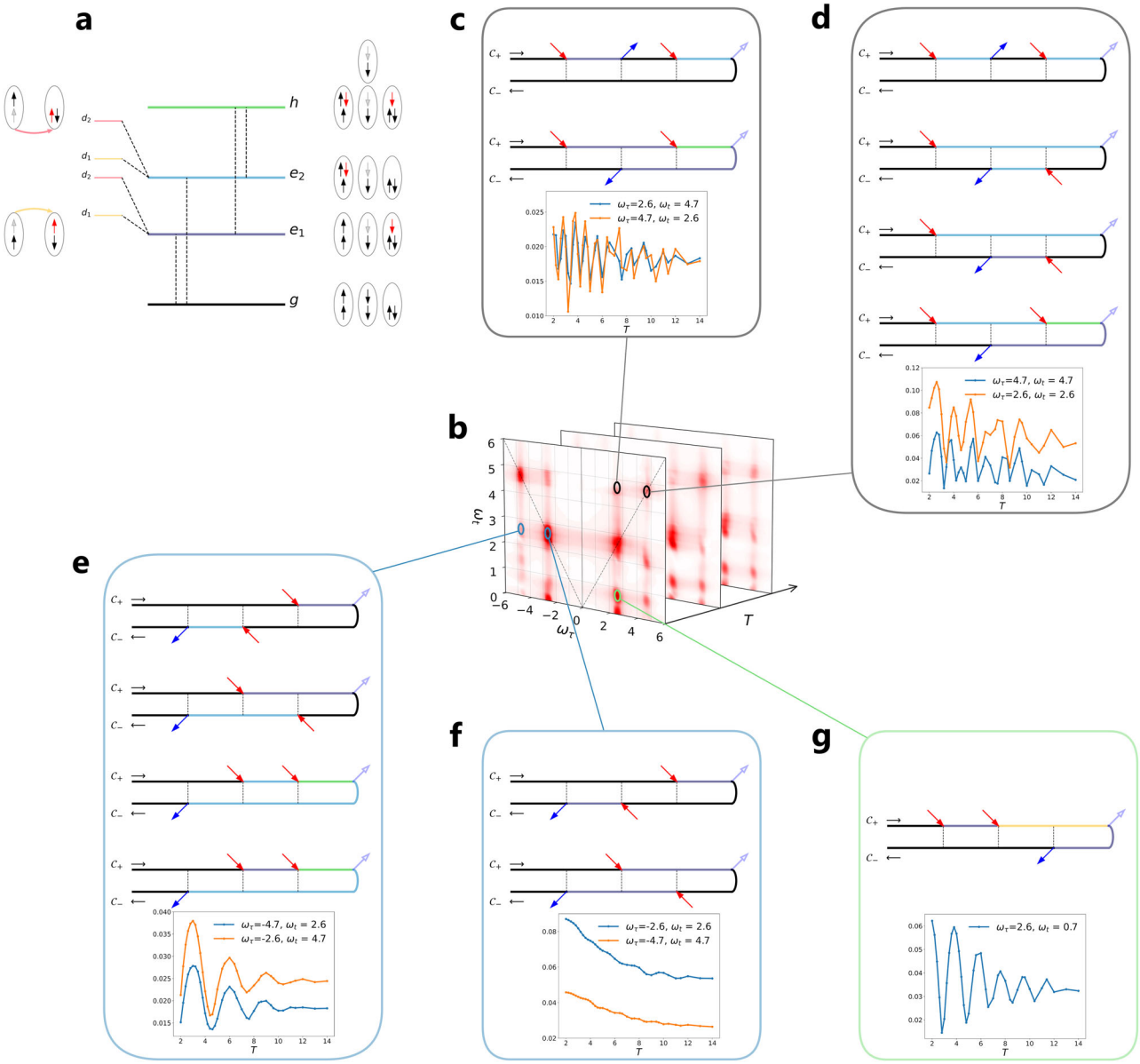

Fig. 4 | 2DCS of a two-orbital Hubbard model near a spin-state transition. **a** Relevant configurations for the spin crossover model: ground state g, excited state e_1, e_2, doubly excited state d_1,d_2, possible high energy state h. **b** 2DCS signal for a given waiting time T. **c**–**g** Signal intensity as a function of T and corresponding contour diagrams corresponding to the blue lines for the NR off-diagonal cross peak (**c**), NR diagonal peak (**d**), R off-diagonal cross peak (**e**), R diagonal peak (**f**) and 2Q signal (**g**). Orange lines share the properties of the blue lines, but correspond to a different excitation process (e_1 or e_2).

doping pulse and the sequence of pump pulses. The signals located at $\omega_\tau = \pm 4.7$ become negative, revealing the bleaching effect of the photo-doping pulse, which transfers population from the g state to the e state. The positive signals indicate the third order response of e. In particular, the signals located at the columns $\omega_\tau = \pm J = \pm 0.7$ ($\pm 3J = \pm 2.1$) represent the injection of the corresponding energies by the first pump (gray circles). Such excitations become possible, because the photo-doped nonequilibrium state contains a significant population of singly and triply occupied sites (see excitations from e to d_1 and e to d_2 in Fig. 5d). Dominant signals associated with such processes appear at emission energy $\omega_t = U = 4$ and $\omega_t = U - 2J = 2.6$, see Keldysh diagrams in Fig. 5e, f). The signal at $\omega_\tau \sim 0$ and $\omega_t = 4.7$ reveals the metallic nature of the photo-induced transient state (black box).

Discussion

We showed how the 2DCS signals of correlated lattice models can be calculated with NEQ-DMFT and interpreted in terms of Keldysh diagrams for few-level systems representing quasi-local processes. An advantage of the real-time approach with explicit simulation of pump pulses is that it allows to calculate nonlinear responses without the explicit evaluation of higher-order correlation functions, and that it can be used to explore the properties of nonequilibrium states. The 2DCS signals reveal information on the nature of the ground state, the excitation or relaxation processes and the coherence times, which are difficult to obtain from standard absorption, conductivity or photoemission spectroscopy measurements. For example, the 2DCS spectra can clearly distinguish a simple Mott insulator from a correlated band insulator with dimerization, because the more complex energy level structure of the latter system leads to a much richer 2DCS signal. Similarly, the 2DCS spectra of multi-orbital Mott systems clearly reveal the relevant interaction parameters U and J, and the activation of new degrees of freedom (like mobile singlons and triplons) in a photo-doped Mott state.

2DCS can measure nonlinear responses with a series of weak probe pulses, which do not significantly perturb the probed many-body state. In the present study, we have focused on a collinear setup within a Bethe-lattice-

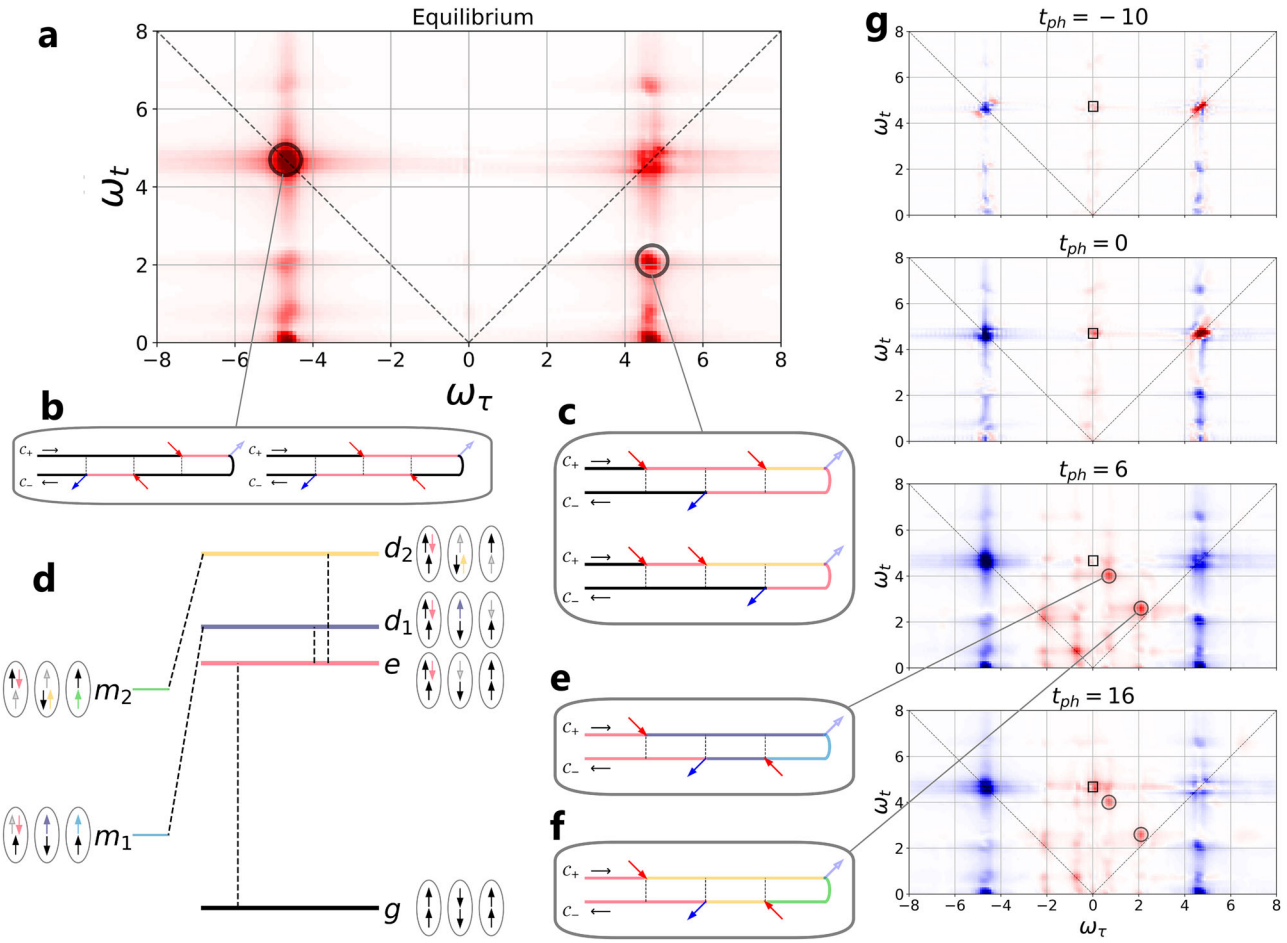

Fig. 5 | 2DCS of a photo-doped two-orbital Hubbard model. a Equilibrium 2DCS signal for the high-spin insulator. **b**, **c** Keldysh diagrams of prominent signals. **d** Spin configurations for the ground state g, excited state e, doubly excited states d_1,d_2 and metastable states m_1,m_2. **e**, **f** Keldysh diagrams of relevant signals in the difference spectrum. **g** 2DCS difference spectra for a photo-doped system at the indicated pump delay times $t_{\rm ph} = -10$, 0, 6 and 16 relative to the 2DCS measurement.

type construction that does not exploit the polarization of the light. In more realistic simulations, additional information could be obtained by varying the geometry, polarization vectors, and relative phases of the pump pulses.

Methods

Nonequilibrium dynamical mean-field theory

Given a time dependent Hamiltonian $\hat{H}(t)$, a contour ordered correlation function on the three-leg Kadanoff-Baym contour $\mathcal{C}$ is defined as[30]

$$C_{AB}(t,t') = \langle \mathcal{T}_{\mathcal{C}} \hat{A}(t)\hat{B}(t')\rangle = \frac{1}{Z}\mathrm{Tr}\left[\mathcal{T}_{\mathcal{C}} e^{-i\int_{\mathcal{C}} d\bar{t}\hat{H}(\bar{t})}\hat{A}(t)\hat{B}(t')\right]. \quad (2)$$

Here, $\mathcal{T}_{\mathcal{C}}$ denotes the contour time ordering operator. The integral over the Matsubara-branch of the three-leg contour, divided by the partition sum Z, corresponds to the density matrix of the initial state.

Using a cavity construction, dynamical mean field theory (DMFT) maps the lattice problem to an effective impurity model with a self-consistently determined bath, represented in action form by the hybridization function $\Delta(t,t')$[48]. The solution of the impurity model yields the impurity Green's function,

$$G(t,t') = -i\frac{1}{Z}\mathrm{Tr}\left[\mathcal{T}_{\mathcal{C}} e^{-i\int_{\mathcal{C}} d\bar{t}\hat{H}_{\rm loc}(\bar{t}) - i\int_{\mathcal{C}} d\bar{t}d\bar{t}' c^\dagger(\bar{t})\Delta(\bar{t},\bar{t}')c(\bar{t}')}\hat{c}^\dagger(t)\hat{c}(t')\right], \quad (3)$$

where for simplicity, we omitted spin and orbital indices. The DMFT self-consistency loop defines Δ in such a way that the impurity Green's function becomes identical to the local lattice Green's function. In the case of the infinitely conneced Bethe lattice, one can derive a direct relation between these two functions: $\Delta(t,t') = h(t')G(t,t')h(t)$, where $h(t)$ is the (properly renormalized) nearest-neighbor hopping[48]. We also use such a relation to approximately treat other lattices, like the dimerized chain[39]. The non-cross approximation (NCA) is used as a nonequilibrium impurity solver[49].

Through the self-consistently determined hybridization function, the nonequilibrium DMFT approach captures the time-evolving state of the lattice system, including collective excitations[50]. This distinguishes our nonequilibrium DMFT framework from a non-selfconsistent perturbative treatment of 2DCS, as used for example in ref. 51.

The electric current in the lattice model is given by

$$\boldsymbol{j}(t) = \langle \hat{\boldsymbol{j}}(t)\rangle = ie\sum_{i,j,s} h_{ij}\boldsymbol{R}_{ij}\langle \hat{c}^\dagger_{js}(t)\hat{c}_{is}(t)\rangle = e\sum_{i,j,s} h_{ij}\boldsymbol{R}_{ij}G^<_{ij,s}(t,t), \quad (4)$$

where $\boldsymbol{R}_{ij}$ is the vector connecting site i and j and h_{ij} the corresponding hopping amplitude. It can be directly calculated when the sites i and j are included in the DMFT impurity problem (e. g. for the dimer). The nonequilibrium DMFT estimate for the electric current between impurity (i) and bath (j) sites is[52]

$$\boldsymbol{j}(t) = -ie\sum_{ij}\boldsymbol{R}_{ij}[G_i * \Delta_j]^<(t,t), \quad (5)$$

where $*$ is a convolution on $\mathcal{C}$ and Δ_j is the hybridization function associated with the hopping to j.

Nonlinear current

The current calculated above is nonperturbative and contains the response to the excitation to all orders. To extract the second (2nd) or third (3rd) order contribution to the electric current, we subtract the lower order currents. Applying the three incoming weak laser pulses A, B, C at time $0, \tau$, and $\tau + T$, we thus obtain the second and third order current responses by calculating

$$\begin{aligned} J^{AB}_{2nd}(\tau, t) &\equiv J^{AB}(t+\tau) - J^{A}(t+\tau) - J^{B}(t+\tau), \\ J^{ABC}_{3rd}(\tau, t) &\equiv J^{ABC}(t+\tau+T) \\ &- J^{AB}_{2nd}(t+\tau+T) - J^{AC}_{2nd}(t+\tau+T) - J^{BC}_{2nd}(t+\tau+T) \\ &- J^{A}(t+\tau+T) - J^{B}(t+\tau+T) - J^{C}(t+\tau+T), \end{aligned} \tag{6}$$

where $J^{X}(\mathscr{T})$ denotes the current measured at time $\mathscr{T}$ in the presence of the pulse combinations $X = A, B, C, AB, BC$, and ABC. A 2D Fourier transformation $t \to \omega_t, \tau \to \omega_\tau$ then yields $J^{AB}_{2nd}(\omega_\tau, \omega_t)$ and $J^{ABC}_{3rd}(\omega_\tau, \omega_t)$. Finally, we take the absolute value $I^{ABC}_{3rd}(\omega_\tau, \omega_t) \equiv |J^{ABC}_{3rd}(\omega_\tau, \omega_t)|$ for the analysis of the spectra.

Electric field pulses

In a gauge with pure vector potential, the effect of an electric field is to dress the hopping amplitudes with a complex Peierls phase $\phi_{ij}(t) = \int_{\boldsymbol{R}_i}^{\boldsymbol{R}_j} \boldsymbol{A}(\boldsymbol{r}, t) d\boldsymbol{r}$,

$$h_{ij}(t) = h_{ij} e^{i\phi_{ij}(t)}. \tag{7}$$

The vector potential itself is the time integral of the electric field of the laser, $\boldsymbol{A}(\boldsymbol{r}, t) = -\int_0^t dt' \boldsymbol{E}(\boldsymbol{r}, t')$. To generate a broad band excitation for 2DCS, we use a broadened delta function in time as the vector potential $A(t) = A_0 \frac{1}{\sqrt{2\pi}\sigma} e^{-\frac{(t-t_0)^2}{2\sigma^2}}$. Specifically, we use $\sigma = 0.2$ for the single-orbital Hubbard model and correlated dimer model, and $\sigma = 0.25$ for the two-orbital Hubbard model. The corresponding power spectrum of the electric field is $|E(\omega)|^2 = A_0 \omega e^{-\sigma^2\omega^2}$.

For the photo-doping in the transient 2DCS simulations, we employ a strong multi-cycle electric field pulse

$$E(t) = E_0 \frac{1}{\sqrt{2\pi}\sigma} e^{-\frac{(t-t_0)^2}{2\sigma^2}} \sin(\omega_0 (t - t_0)). \tag{8}$$

Here, the pulse frequency ω_0 (comparable to the gap size) is chosen to maximize absorption and the width of the envelope σ is large enough to accommodate multiple cycles.

Data availability

Data for the manuscript or supplementary information is provided upon reasonable request.

Received: 22 December 2024; Accepted: 22 April 2025;
Published online: 09 May 2025

References

1. Schultze, M. et al. Controlling dielectrics with the electric field of light. *Nature* **493**, 75–78 (2013).
2. Giannetti, C. et al. Ultrafast optical spectroscopy of strongly correlated materials and high-temperature superconductors: a non-equilibrium approach. *Adv. Phys.* **65**, 58–238 (2016).
3. de la Torre, A. et al. Colloquium: Nonthermal pathways to ultrafast control in quantum materials. *Rev. Mod. Phys.* **93**, 041002 (2021).
4. Okamoto, H. et al. Ultrafast charge dynamics in photoexcited Nd_2CuO_4 and La_2CuO_4 cuprate compounds investigated by femtosecond absorption spectroscopy. *Phys. Rev. B* **82**, 060513 (2010).
5. Boschini, F., Zonno, M. & Damascelli, A. Time-resolved arpes studies of quantum materials. *Rev. Mod. Phys.* **96**, 015003 (2024).
6. Mukamel, S. *Principles of Nonlinear Optical Spectroscopy* (Oxford University Press, 1995).
7. Mukamel, S. Multidimensional Femtosecond Correlation Spectroscopies of Electronic and Vibrational Excitations. *Annu. Rev. Phys. Chem.* **51**, 691–729 (2000).
8. Hamm, P. & Zanni, M. *Concepts and Methods of 2D Infrared Spectroscopy* (Cambridge University Press, Cambridge, 2011).
9. Mahmood, F., Chaudhuri, D., Gopalakrishnan, S., Nandkishore, R. & Armitage, N. P. Observation of a marginal Fermi glass. *Nat. Phys.* **17**, 627–631 (2021).
10. Zhang, S. et al. Revealing the frequency-dependent oscillations in the nonlinear terahertz response induced by the Josephson current. *Natl Sci. Rev.* **10**, nwad163 (2023).
11. Barbalas, D. et al. Energy Relaxation and dynamics in the correlated metal Sr_2RuO_4 via THz two-dimensional coherent spectroscopy. Preprint at https://arxiv.org/abs/2312.13502 (2023).
12. Liu, A. et al. Probing inhomogeneous cuprate superconductivity by terahertz Josephson echo spectroscopy. *Nat. Phys.* **20**, 1–6 (2024).
13. Liu, A. Multidimensional terahertz probes of quantum materials. *npj Quantum Mater.* **10**, 18 (2025).
14. Zhang, Z. et al. Terahertz-field-driven magnon upconversion in an antiferromagnet. *Nat. Phys.* **20**, 1–6 (2024).
15. Gómez Salvador, A. et al. Principles of two-dimensional terahertz spectroscopy of collective excitations: The case of Josephson plasmons in layered superconductors. *Phys. Rev. B* **110**, 094514 (2024).
16. Li, X., Zhang, T., Borca, C. N. & Cundiff, S. T. Many-Body Interactions in Semiconductors Probed by Optical Two-Dimensional Fourier Transform Spectroscopy. *Phys. Rev. Lett.* **96**, 057406 (2006).
17. Moody, G. et al. Intrinsic homogeneous linewidth and broadening mechanisms of excitons in monolayer transition metal dichalcogenides. *Nat. Commun.* **6**, 8315 (2015).
18. Yue, L. et al. Giant nonlinear optical wave mixing in a van der Waals correlated insulator. *Sci. Adv.* **10**, eadn6216 (2024).
19. Wan, Y. & Armitage, N. P. Resolving Continua of Fractional Excitations by Spinon Echo in THz 2D Coherent Spectroscopy. *Phys. Rev. Lett.* **122**, 257401 (2019).
20. Li, Z.-L., Oshikawa, M. & Wan, Y. Photon Echo from Lensing of Fractional Excitations in Tomonaga-Luttinger Spin Liquid. *Phys. Rev. X* **11**, 031035 (2021).
21. Gao, Q., Liu, Y., Liao, H. & Wan, Y. Two-dimensional coherent spectrum of interacting spinons from matrix product states. *Phys. Rev. B* **107**, 165121 (2023).
22. Li, Z.-L. & Wan, Y. Photon echo and fractional excitation lensing of the S = 1/2 XY spin chain. *Phys. Rev. B* **108**, 165151 (2023).
23. Li, Z.-L., Li, X.-H. & Wan, Y. Time-domain interferometry of electron weak localization through terahertz nonlinear response. *Phys. Rev. Res.* **6**, 033125 (2024).
24. Choi, W., Lee, K. H. & Kim, Y. B. Theory of Two-Dimensional Nonlinear Spectroscopy for the Kitaev Spin Liquid. *Phys. Rev. Lett.* **124**, 117205 (2020).
25. Sim, G., Knolle, J. & Pollmann, F. Nonlinear spectroscopy of bound states in perturbed Ising spin chains. *Phys. Rev. B* **107**, L100404 (2023).
26. Sim, G., Pollmann, F. & Knolle, J. Microscopic details of two-dimensional spectroscopy of one-dimensional quantum Ising magnets. *Phys. Rev. B* **108**, 134423 (2023).
27. Phuc, N. T. & Trung, P. Q. Direct and ultrafast probing of quantum many-body interactions through coherent two-dimensional spectroscopy: From weak- to strong-interaction regimes. *Phys. Rev. B* **104**, 115105 (2021).

28. Watanabe, Y., Trebst, S. & Hickey, C. Exploring Two-dimensional Coherent Spectroscopy with Exact Diagonalization: Spinons and Confinement in 1D Quantum Magnets. *Phys. Rev. B* **110**, 134443 (2024).
29. Qiang, Y., Quito, V. L., Trevisan, T. V. & Orth, P. P. Probing Majorana Wave Functions in Kitaev Honeycomb Spin Liquids with Second-Order Two-Dimensional Spectroscopy. *Phys. Rev. Lett.* **133**, 126505 (2024).
30. Aoki, H. et al. Nonequilibrium dynamical mean-field theory and its applications. *Rev. Mod. Phys.* **86**, 779–837 (2014).
31. Vidas, L. et al. Does VO_2 Host a Transient Monoclinic Metallic Phase? *Phys. Rev. X* **10**, 031047 (2020).
32. Ligges, M. et al. Ultrafast doublon dynamics in photoexcited 1*T*-TaS_2. *Phys. Rev. Lett.* **120**, 166401 (2018).
33. Chen, J., Petocchi, F., Christiansson, V. & Werner, P. Nature of the photoinduced metallic state in monoclinic VO_2. *Phys. Rev. B* **109**, L201101 (2024).
34. Brańczyk, A. M., Turner, D. B. & Scholes, G. D. Crossing disciplines - A view on two-dimensional optical spectroscopy. *Ann. Der Phys.* **526**, 31–49 (2014).
35. Bakulin, A. A., Silva, C. & Vella, E. Ultrafast Spectroscopy with Photocurrent Detection: Watching Excitonic Optoelectronic Systems at Work. *J. Phys. Chem. Lett.* **7**, 250–258 (2016).
36. Hansen, T. & Pullerits, T. Nonlinear response theory on the Keldysh contour. *J. Phys. B At. Mol. Optical Phys.* **45**, 154014 (2012).
37. Biermann, S., Poteryaev, A., Lichtenstein, A. I. & Georges, A. Dynamical singlets and correlation-assisted peierls transition in VO_2. *Phys. Rev. Lett.* **94**, 026404 (2005).
38. Ritschel, T., Berger, H. & Geck, J. Stacking-driven gap formation in layered 1*T*-TaS_2. *Phys. Rev. B* **98**, 195134 (2018).
39. Petocchi, F., Chen, J., Li, J., Eckstein, M. & Werner, P. Photoinduced charge dynamics in 1*T*-TaS_2. *Phys. Rev. B* **107**, 165102 (2023).
40. Petocchi, F. et al. Mott versus hybridization gap in the low-temperature phase of 1*T*-TaS_2. *Phys. Rev. Lett.* **129**, 016402 (2022).
41. Lee, S.-H., Goh, J. S. & Cho, D. Origin of the insulating phase and first-order metal-insulator transition in 1*T*-TaS_2. *Phys. Rev. Lett.* **122**, 106404 (2019).
42. Werner, P., Strand, H. U. R., Hoshino, S. & Eckstein, M. Ultrafast switching of composite order in A_3C_{60}. *Phys. Rev. B* **95**, 195405 (2017).
43. Werner, P. & Millis, A. J. High-spin to low-spin and orbital polarization transitions in multiorbital mott systems. *Phys. Rev. Lett.* **99**, 126405 (2007).
44. Sensarma, R. et al. Lifetime of double occupancies in the Fermi-Hubbard model. *Phys. Rev. B* **82**, 224302 (2010).
45. Strohmaier, N. et al. Observation of elastic doublon decay in the fermi-hubbard model. *Phys. Rev. Lett.* **104**, 080401 (2010).
46. Eckstein, M. & Werner, P. Thermalization of a pump-excited mott insulator. *Phys. Rev. B* **84**, 035122 (2011).
47. Hamm, P. Transient 2D IR spectroscopy from micro- to milliseconds. *J. Chem. Phys.* **154**, 104201 (2021).
48. Georges, A., Kotliar, G., Krauth, W. & Rozenberg, M. J. Dynamical mean-field theory of strongly correlated fermion systems and the limit of infinite dimensions. *Rev. Mod. Phys.* **68**, 13–125 (1996).
49. Eckstein, M. & Werner, P. Nonequilibrium dynamical mean-field calculations based on the noncrossing approximation and its generalizations. *Phys. Rev. B* **82**, 115115 (2010).
50. Chen, J., Tsuji, N. & Werner, P. Higgs mode in two-dimensional coherent spectroscopy of weak-coupling antiferromagnets. Preprint at https://arxiv.org/abs/2504.21351 (2025).
51. Sun, H., Harbola, U., Mukamel, S. & Galperin, M. Two-Dimensional Spectroscopy of Open Quantum Systems: Nonequilibrium Green's Function Formulation. *J. Phys. Chem. Lett.* **16**, 2008–2015 (2025).
52. Lysne, M., Murakami, Y. & Werner, P. Signatures of bosonic excitations in high-harmonic spectra of mott insulators. *Phys. Rev. B* **101**, 195139 (2020).

Acknowledgements

We thank M. Eckstein and F. Petocchi for helpful discussions. J.C. also thanks Z. Li and Y. Wan for motivating discussions. This work was supported by the Swiss National Science Foundation through the Research Unit QUAST of Deutsche Foschungsgemeinschaft (FOR5249), and Grant No. 200021-196966. The calculations were performed on the Beo05 cluster at the University of Fribourg.

Author contributions

J.C. performed the calculations. P.W. conceived and supervised the project. Both authors analyzed the data and wrote the paper.

Competing interests

The authors declare no competing interests.

Additional information

Supplementary information The online version contains supplementary material available at https://doi.org/10.1038/s41524-025-01619-0.

Correspondence and requests for materials should be addressed to Philipp Werner.